

Banner appropriate to article type will appear here in typeset article

# Direct numerical simulations of optimal thermal convection in rotating plane layer dynamos.

Souvik Naskar<sup>1</sup>, Anikesh Pal<sup>1</sup>†

<sup>1</sup>Department of Mechanical Engineering, Indian Institute of Technology, Kanpur 208016, India

(Received xx; revised xx; accepted xx)

The heat transfer behavior of convection-driven dynamos in a rotating plane layer between two parallel plates, heated from the bottom and cooled from the top, is investigated. At a fixed rotation rate (Ekman Number,  $E = 10^{-6}$ ) and fluid properties (thermal and magnetic Prandtl numbers,  $Pr = Pr_m = 1$ ), both dynamo convection (DC) and non-magnetic rotating convection (RC) simulations are performed to demarcate the effect of magnetic field on heat transport at different thermal forcing (Rayleigh Number,  $Ra = 3.83 \times 10^9 - 3.83 \times 10^{10}$ ). In this range, our turbulence resolving simulations demonstrate the existence of an optimum thermal forcing, at which heat transfer between the plates in DC exhibits maximum enhancement, as compared to the heat transport in the RC simulations. Unlike any global force balance reported in the literature, the present simulations reveal an increase in the Lorentz force in the *thermal boundary layer*, due to stretching of magnetic field lines by the vortices near the walls with no-slip boundary condition. This increase in Lorentz force mitigates turbulence suppression owing to the Coriolis force, resulting in enhanced turbulence and heat transfer.

**Key words:**

## 1. Introduction

Hydromagnetic dynamo action is the commonly accepted source of sustained magnetic fields in stars and planets. In this mechanism, a convective system with electrically conducting fluid can amplify a small magnetic field and continuously convert the kinetic energy of the fluid to magnetic energy, to sustain the field against Joule dissipation. This self-exciting dynamo action can be facilitated due to the presence of rotation leading to large-scale organized fields (Moffatt & Dormy 2019). The most familiar example of such a rotating convection-driven dynamo is the Earth's outer core, where the dynamo mechanism originating from the turbulent motions of electrically conducting liquid iron in Earth's outer core forms the sustained dipole dominant geomagnetic field (Roberts & King 2013). Thermal convection in rotating dynamos, both in plane layer (Stellmach & Hansen 2004; Tilgner 2012) and spherical (Glatzmaiers & Roberts 1995; Christensen & Wicht 2015) geometries, have been extensively investigated to understand their force balance, nature of MHD turbulence, and

† Email address for correspondence: pala@iitk.ac.in

magnetic field behavior. Another aspect of fundamental importance is the heat transfer to diagnose the global transport properties of such systems. Convective heat transfer through the atmosphere decides the weather, climate, planetary and stellar energetics, their evolution (Schmitz & Tilgner 2009), and generation of magnetic fields from planetary cores (Nimmo 2015). However, heat transport in self-excited rotating dynamos is yet to be explored.

Dynamics of flow and heat transfer in thermal convection with rotation and magnetic field depends on four governing non-dimensional numbers: (I) the Rayleigh Number ( $Ra$ ) representing the thermal forcing, (II) the Ekman Number ( $E$ ) signifying the ratio of viscous force to Coriolis force, (III) the thermal Prandtl number ( $Pr$ ) and (IV) the magnetic Prandtl number ( $Pr_m$ ).  $Pr$  and  $Pr_m$  are fluid properties as defined in equation 2.5. These four numbers decide the global characteristics of the system, indicated by (a) the magnetic Reynolds Number ( $Re_m = u_{r.m.s}d/\lambda$ , where  $u_{r.m.s}$  and  $d$  are the characteristics velocity and length scales, whereas  $\lambda$  is the magnetic diffusivity), characterizing the dominance of electromagnetic induction over ohmic diffusion of the magnetic field, (b) the Nusselt Number ( $Nu$ ) representing non-dimensional heat transfer (see equation 2.9) and, (c) the Elsasser Number ( $\Lambda = \sigma B_{r.m.s}^2/\rho\Omega$ , where  $\sigma$  is the electrical conductivity,  $B_{r.m.s}$  is the characteristics magnetic field strength,  $\rho$  is the density, and  $\Omega$  is the rotation rate), depicting the ratio of the Lorentz and the Coriolis forces.

Based on the behavior of magnetic field with varying  $Re_m$ , thermal convection with rotation and magnetic field can be broadly classified into two categories: (I) rotating magnetoconvection (RMC) at low magnetic Reynolds number ( $Re_m \rightarrow 0$ ) and (II) dynamo convection (DC) for moderate to high values  $Re_m \geq O(10)$ . For RMC, the system can not self-induce or sustain a magnetic field, and therefore the magnetic field has to be imposed externally. As the self-induced magnetic field remains small with respect to the imposed field, linear analysis may be used to predict the critical value of Rayleigh number ( $Ra_c$ ) at the onset of convection (Chandrasekhar 1961). Moreover, liquid metals (e.g. Mercury, Sodium, Gallium), having large magnetic diffusivities ( $\lambda \rightarrow O(10^6 - 10^7)$ ) are used to conduct RMC experiments at low  $Re_m$ . Strong rotation in any convective system restricts convection, attributed to the Taylor-Proudman constraint imposed by the Coriolis force, which inhibits changes along the axis of rotation. Linear theory of RMC (Chandrasekhar 1961) suggests that magnetic field can relax Taylor-Proudman constraint to enhance convection, known as the "magnetorelaxation" process. These theoretical predictions have been verified by experiments (Nakagawa 1957, 1959; Aurnou & Olson 2001). Eltayeb (1972) performed an extensive linear analysis of RMC in the asymptotic limits of large rotation rate ( $E \rightarrow 0$ ) with large imposed field strength for various boundary conditions, orientations of the external magnetic field, and rotation. Later, the linear theory was extended to allow for finite-amplitude modes considering the dominant modes contribute to most of the heat transport (Stevenson 1979). In RMC, the action of Lorentz force on the flow can lead to enhanced heat transfer (King & Aurnou 2015) as compared to non-magnetic rotating convection (RC). The highest enhancement occurs when the Lorentz force due to the magnetic field and the Coriolis force due to rotation balance each other, as found in the experiment of King & Aurnou (2015). This global balance, known as the "magnetostrophic" state, is characterized by Elsasser number of order unity,  $\Lambda \approx O(1)$ .

Challenges in producing dynamo action in laboratory experiments (Plumley & Julien 2019) compel the studies on turbulent dynamo convection (DC) to depend primarily on numerical simulations. Self-exciting dynamo simulations at moderate values of magnetic Reynolds number ( $Re_m = 243 - 346$ ) in a spherical shell model performed by Yadav

*et al.* (2016), revealed a fundamentally different force balance compared to the experimental results of King & Aurnou (2015). In such "geodynamo" simulations that attempt to model the Earth's outer core, the primary force balance is "geostrophic" between Coriolis and pressure forces, whereas the Magnetic, the Archemedian (buoyancy), and the Coriolis forces (MAC) constitute a lower order of magnitude (quasi-geostrophic, QG) balance, abbreviated as the QG-MAC balance (Aubert 2019; Schwaiger *et al.* 2019). Interestingly, Yadav *et al.* (2016) also reported a similar heat transfer enhancement as found in the RMC experiments of King & Aurnou (2015), irrespective of very different force balance and parameter regime.

The present study explores the heat transfer behavior in DC with a plane layer geometry using direct numerical simulations (DNS). This is the simplest possible model of DC in a rotating layer of electrically conducting fluid between two parallel plates, heated from the bottom and cooled from the top (see figure 1a). Using this model, Jones & Roberts (2000) investigated the effect of  $Ra$ ,  $E$ , and  $Pr_m$  on the growth and saturation of the magnetic field and the global force balance while neglecting inertial effects at large Prandtl numbers ( $Pr \rightarrow \infty$ ). The dynamo was found to saturate at  $\Lambda \approx O(1)$ . At moderate values of magnetic Reynolds number,  $Re_m \approx O(10^2)$  a simple model of dynamo convection was proposed. Rotvig & Jones (2002) studied DC in the range  $E = 10^{-4} - 10^{-5}$  and reported a MAC balance in the bulk with  $\Lambda \approx O(10)$ . Rapidly rotating ( $E = 2 \times 10^{-4} - 10^{-6}$ ), weakly non-linear DC was explored by Stellmach & Hansen (2004). They reported time-dependent flow with cyclic variation between small and large-scale magnetic fields. Interestingly, dynamo action was found to exist even below the critical Rayleigh number for the onset of non-magnetic convection ( $Ra_c$ ), indicating subcritical dynamo action. Cattaneo & Hughes (2006) analyzed the  $\alpha$ -effect (a mechanism of large-scale field generation from small-scales due to the helical nature of the flow in DC (Moffatt & Dormy 2019)) and reported small-scale dynamos with a diffusively controlled  $\alpha$ -effect, without any indication of large-scale field generation. A transition between small-scale and large-scale field generation was found by Tilgner (2012, 2014) with separate scaling laws for the magnetic energy. The transition occurs at  $Re_mE^{1/3} = 13.5$ , below which the magnetic field generation is dependent on flow helicity. Equipartition of energies is observed above the transition point where the field stretching process at high  $Re_m$  generates small-scale fields independent of flow helicity. Guervilly *et al.* (2015) demonstrated the existence of large-scale vortices in DC that can lead to large-scale field generation, which is of great interest for astrophysical dynamos. These vortices reduced the heat transfer efficiency. However, for high  $Re_m$ , generation of small-scale magnetic field suppresses the formation of such vortices (Guervilly *et al.* 2017). Calkins *et al.* (2015) investigated asymptotically reduced DC models with leading order QG balance. Four distinct QG dynamo regimes have been identified with varying dynamics and magnetic to kinetic energy density ratios (Calkins 2018). Extension to non-Boussinesq convection was investigated by Käpylä *et al.* (2009) and Favier & Bushby (2013).

The heat transport behavior in plane layer DC remains almost unexplored. In this geometry, two distinct regions of convection can be identified: the boundary layer region near the plates with high velocity and temperature gradients (Ekman and thermal boundary layers) and a well-mixed "bulk" regime in the interior where gradients are much smaller. Heat transfer scaling of dynamos without rotation has been found to be identical to non-rotating, non-magnetic Rayleigh Bénard convection (Yan *et al.* 2021), where heat transfer is known to be constrained by the boundary layer dynamics (Plumley & Julien 2019). Conversely, heat transfer in non-magnetic rotating convection is constrained by the bulk, though it can be significantly altered by the boundary layer dynamics (Stellmach *et al.* 2014). Even without considering the viscous boundary layer, Stellmach & Hansen (2004) found enhanced heat

transfer in weakly non-linear convection in a rapidly rotating dynamo. They attributed this increased heat transport to the increased length scale of convection due to the presence of a strong magnetic field. However, the variation of heat transfer with thermal forcing in a rotating dynamo remains unknown. Also, to the best of our knowledge, no studies report the role of the boundary layer on the heat transfer behavior in rotating DC. We perform a systematic study, unprecedented to the previous investigations, in a plane layer geometry to investigate the boundary layer dynamics of dynamos and its implications on the heat transfer behavior.

## 2. Method

### 2.1. Governing equations and numerical details

We consider dynamo convection in a three-dimensional Cartesian layer of incompressible, electrically conducting, Boussinesq fluid. The layer of depth  $d$  is kept between two parallel plates with temperature difference  $\Delta T$  where the lower plate is hotter (see figure 1a). The system is rotating about the vertical with an angular velocity  $\Omega$ . The fluid properties are density( $\rho$ ), kinematic viscosity( $\nu$ ), thermal diffusivity( $\kappa$ ), magnetic permeability( $\mu$ ), electrical conductivity( $\sigma$ ) and the magnetic diffusivity( $\lambda$ ). The layer depth  $d$  is the length scale, free-fall velocity,  $u_f = \sqrt{g\alpha\Delta Td}$ , is the velocity scale,  $\sqrt{\rho\mu}u_f$  is the magnetic field scale and the temperature drop across the layer,  $\Delta T$  is the temperature scale assumed for non-dimensionalizing the governing equations (Iyer *et al.* 2020). The non-dimensional equations for the velocity field  $\mathbf{u}$ , temperature field  $\theta$ , and magnetic field  $\mathbf{B}$ , take the following form:

$$\frac{\partial u_j}{\partial x_j} = \frac{\partial B_j}{\partial x_j} = 0, \quad (2.1)$$

$$\frac{\partial u_i}{\partial t} + u_j \frac{\partial u_i}{\partial x_j} = -\frac{\partial p}{\partial x_i} + \frac{2}{E} \sqrt{\frac{Pr}{Ra}} \epsilon_{ij3} u_j \hat{e}_3 + B_j \frac{\partial B_i}{\partial x_j} + \theta \delta_{i3} + \sqrt{\frac{Pr}{Ra}} \frac{\partial^2 u_i}{\partial x_j \partial x_j}, \quad (2.2)$$

$$\frac{\partial \theta}{\partial t} + u_j \frac{\partial \theta}{\partial x_j} = \frac{1}{\sqrt{RaPr}} \frac{\partial^2 \theta}{\partial x_j \partial x_j}, \quad (2.3)$$

$$\frac{\partial B_i}{\partial t} + u_j \frac{\partial B_i}{\partial x_j} = B_j \frac{\partial u_i}{\partial x_j} + \sqrt{\frac{Pr}{Ra}} \frac{1}{Pr_m} \frac{\partial^2 B_i}{\partial x_j \partial x_j}. \quad (2.4)$$

The non-dimensional parameters appearing in equations [2.2-2.4] are defined below:

$$Ra = \frac{g\alpha\Delta Td^3}{\kappa\nu}, \quad E = \frac{\nu}{\Omega d^2}, \quad Pr = \frac{\nu}{\kappa}, \quad Pr_m = \frac{\nu}{\lambda}. \quad (2.5)$$

In the horizontal directions ( $x_1, x_2$ ) periodic boundary conditions are applied. The velocity boundary conditions are no-slip and impenetrable. As we aim to study the effect of boundary layer dynamics on dynamo convection, the no-slip boundary condition is the natural choice (Stellmach *et al.* 2014; Jones & Roberts 2000). Although corresponding results for free-slip boundary condition are also presented, we discuss the results for no-slip boundary condition unless stated otherwise. Therefore,

$$u_1 = u_2 = u_3 = 0 \quad \text{at} \quad x_3 = \pm 1/2 \quad (2.6)$$

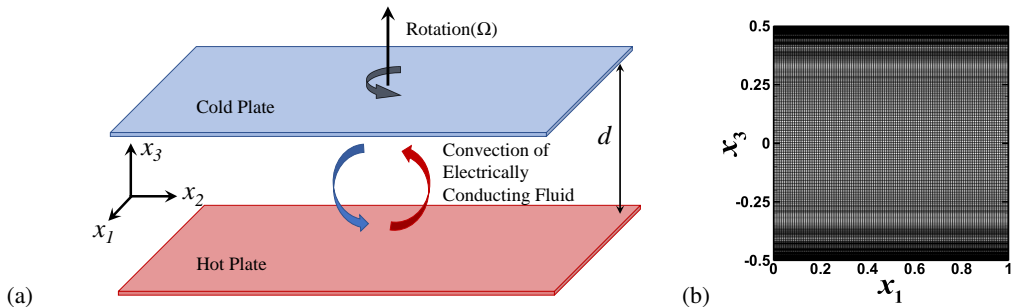


Figure 1: (a) Plane layer dynamo model (b) Grid clustering near the walls to resolve boundary layers

An unstable temperature gradient is maintained by imposing isothermal boundary conditions.

$$\theta = 1 \text{ at } x_3 = -1/2, \quad \theta = 0 \text{ at } x_3 = 1/2 \quad (2.7)$$

For the magnetic field, either perfectly conducting or perfectly insulating boundary conditions can be implemented. The insulating boundary condition is commonly applied in spherical shell geometries for geodynamo simulations (Yadav *et al.* 2016; Christensen & Wicht 2015). However, for plane layer geometries, perfectly conducting boundary condition is commonly used (Tilgner 2012; Guervilly *et al.* 2015; Hughes & Cattaneo 2019) because it enables comparison with the theoretical studies (Stellmach & Hansen 2004). Laboratory setups for RMC (King & Aurnou 2015) and dynamos (Monchaux *et al.* 2007) also use conducting materials as containers of liquid metals that are commonly used to conduct experiments. Thus, perfectly conducting boundary condition are implemented in the present study such that,

$$\frac{\partial B_1}{\partial x_3} = \frac{\partial B_2}{\partial x_3} = 0, \quad B_3 = 0 \text{ at } x_3 = \pm 1/2. \quad (2.8)$$

The governing equations are solved in a cubic domain with unit side length, using the finite difference method (Bakhuis *et al.* 2018) in a staggered grid arrangement. The scalar quantities (pressure and temperature) are stored at the cell centers whereas, velocity and magnetic field components are stored at the cell faces. Second-order central difference is used for spatial discretization. The projection method is used to calculate the divergence-free velocity field where the pressure Poisson equation is solved using a parallel multigrid algorithm. Similarly, an elliptic divergence cleaning algorithm is employed to keep the magnetic field solenoidal (Brackbill & Barnes 1980). An explicit third-order Runge-Kutta method is used for time advancement except for the diffusion terms, which are solved implicitly using the Crank-Nicolson method (Pham *et al.* 2009; Brucker & Sarkar 2010). The solver has been validated extensively for numerous DNS of stratified turbulent flows (Pal *et al.* 2013; Pal & Sarkar 2015; Pal & Chalamalla 2020).

Validation of our numerical solver is performed by replicating the results from the following literature: (I) critical Rayleigh number and wavenumber ( $Ra_c$  and  $a_c$ ) at the onset of non-rotating magnetoconvection with imposed field strength  $Q = \sigma B^2 d^2 / \rho \nu = 10^{-4}$  predicted from linear theory (Chandrasekhar 1961), (II) RC simulations of Stellmach &

---

	$Ra_c$	$a_c$	$Nu_q$	$Re_q$	$Re_0$	$Nu_0$	$Re_m$	$Nu$	$\Lambda$	$ER$
Chandrasekhar (1961)	124509	8.66	-	-	-	-	-	-		
Validation I	124510	8.47								
Stellmach & Hansen (2004)	-	-	-	-	48.3	1.34	170.7	1.66	0.38	1.37
Validation II					48.6	1.36	168.5	1.68	0.36	1.36
Yan <i>et al.</i> (2019)	-	-	1.149	3.79	-	-	-	-		
Validation III			1.149	3.72						

---

Table 1: Results from the three test runs to reproduce results from literatures: (I) Linear magnetoconvection theory (Chandrasekhar 1961), (II) RC and DC simulations of Stellmach & Hansen (2004) and (III) DNS results of quasi-static magnetoconvection (Yan *et al.* 2019). Subscript "0" and  $q$  are used to represent non-magnetic RC and quasi-static magnetoconvection results respectively. The magnetic to kinetic energy ratio is represented by  $ER$ .

---

Hansen (2004) at  $Ra = 1.4 \times 10^7$ ,  $E = 5 \times 10^{-5}$  and  $Pr = 1$ , along with DC simulation results for  $Pr_m = 2.5$  with free-slip boundary conditions, (III) DNS results of quasi-static magnetoconvection (Yan *et al.* 2019) at  $Q = 10^{-4}$  and  $Ra = 1.3 \times 10^5$ . Our results are in good agreement with these earlier studies as demonstrated in table 1.

## 2.2. Problem Setup

Dynamical balances and heat transport are studied at constant rotation rate and constant fluid properties with variation in thermal forcing. The thermal forcing here is represented by the convective supercriticality  $\mathcal{R} = Ra/Ra_c$  where  $Ra_c = 19.15 \times E^{-4/3}$  is the minimum required value of  $Ra$  to start rotating convection (Chandrasekhar 1961) with no-slip boundary conditions (critical Rayleigh Number is higher for free-slip boundaries where  $Ra_c = 21.91 \times E^{-4/3}$  for large rotation rates). We choose the values of  $\mathcal{R} = 2, 2.5, 3, 4, 5, 10, 20$ , Ekman number  $E = 10^{-6}$  and the Prandtl Numbers  $Pr = Pr_m = 1$  for the present simulations. To elucidate the effect of the magnetic field, we perform two simulations at each value of  $\mathcal{R}$ : DC and RC. It should be noted here that the critical Rayleigh number for the onset of dynamo convection remains unknown (Plumley & Julien 2019). Hence, we use the same value of  $Ra_c$  for both DC and RC simulations following Stellmach & Hansen (2004). In the horizontal directions ( $x_1$  and  $x_2$ ) 1024 uniform grid points are used, whereas in the vertical direction ( $x_3$ ) we have used 256 non-uniform grid points. Capturing the boundary layer dynamics in these simulations is imperative for understanding the optimal heat transfer phenomenon, and requires a grid that can resolve the smallest dissipative scales. Grid clustering (Bakhuis *et al.* 2018) near the walls (figure 1b) is performed to ensure a minimum of four grid points inside the Ekman layer with the spacing,  $\Delta x_3 = 4.8 \times 10^{-4}$  at the wall. This grid resolution is selected after subsequent grid refinements such that the kinetic and magnetic energies are sufficiently dissipated, and the turbulent kinetic energy budget closure is maintained. The simulation details and global diagnostic parameters are summarized in table 2.

We start the DC simulations at  $\mathcal{R} = 20$ , by introducing a small magnetic perturbation in a statistically steady RC simulation, as shown in figure 2a. The magnetic field shows an exponential growth over approximately one free decay time scale ( $t_\lambda = d^2/\lambda$ ) before it saturates. The decrease in Reynolds Number ( $Re = Re_m/Pr_m$ ), signify decrease in turbulence due to dynamo action at  $\mathcal{R} = 20$ . Simulations at lower values of  $\mathcal{R}$  are started

---

$\mathcal{R}$	$Ra$	$Re_m$	$\frac{Nu}{Nu_0}$	$\Lambda$	$\Lambda_T$	$Ro_T$
2	$3.8300 \times 10^9$	729	0.7466	0.2186	0.0046	0.0220
2.5	$4.7875 \times 10^9$	1327	1.2550	0.5163	0.2921	0.0484
3	$5.7450 \times 10^9$	2012	1.7205	1.0313	0.6170	0.0727
4	$7.6600 \times 10^9$	2284	1.4941	1.6834	0.5545	0.1211
5	$9.5750 \times 10^9$	2660	1.4282	2.3994	0.4616	0.1535
10	$1.9150 \times 10^{10}$	4203	1.1714	3.7428	0.2137	0.3539
20	$3.8300 \times 10^{10}$	7642	1.1377	13.2865	0.1672	0.8663

---

Table 2: Statistics of the DC simulations with no-slip boundary conditions at  $E = 10^{-6}$ ,  $Pr = Pr_m = 1$

---

using the data of higher  $\mathcal{R}$  as the initial condition to save computational time. The mean magnetic field is calculated to outline the behavior of the dynamos, by averaging the field over horizontal planes. This horizontal averaging of any quantity  $\phi$  is denoted by over-bar in the following discussion, with  $\bar{\phi}$  denoting the mean and  $\phi_{rms}$  representing the *r.m.s.* field. The vertical variation of the mean horizontal magnetic fields ( $\bar{B}_1$  and  $\bar{B}_2$ ) is depicted in figure 2b. It should be noted here that the vertical component of the mean magnetic field ( $\bar{B}_3$ ) is zero everywhere by the definition of averages and solenoidal field conditions. Thus the mean-field remains horizontal. However, as we show later in figure 9b, the vertical component of the *r.m.s.* field ( $b_{3,rms}$ ) is non-zero except at the walls. We observe one order of magnitude drop in the mean-field strength (figure 2b) with increasing  $\mathcal{R}$  signifying a transition from large scale to small scale dynamo action. The magnetic Reynolds number (based on the horizontal scale of convective cells, (Tilgner 2012)) varies as  $Re_mE^{1/3} \approx 7 - 76$  in the range  $\mathcal{R} = 2 - 20$  in our simulations. A similar transition in dynamos is reported to occur at  $Re_mE^{1/3} = 13.5$  (Tilgner 2012, 2014) which lies between  $\mathcal{R} = 2.5 - 3$  our simulations.

In the following discussion, the DC and RC simulations are compared in terms of their heat transfer, and turbulence properties. Heat transfer is represented by the Nusselt number ( $Nu$ ), defined as the total heat to conductive heat transferred from the bottom plate to the top plate. The intensity of turbulence is characterized by the turbulent kinetic energy ( $K$ ), whereas the viscous and the Joule dissipation signifies the conversion of kinetic, and magnetic energy to internal energy via the action of viscous and magnetic diffusion, respectively.

$$\begin{aligned}
 Nu &= \frac{qd}{k\Delta T} = 1 + \sqrt{RaPr}\langle u_3\theta \rangle, & \langle K \rangle &= \left\langle \frac{1}{2}u_i u_i \right\rangle \\
 \langle \epsilon_v \rangle &= \sqrt{\frac{Pr}{Ra}} \left\langle \frac{\partial u_i}{\partial x_j} \frac{\partial u_i}{\partial x_j} \right\rangle, & \langle \epsilon_j \rangle &= \sqrt{\frac{Pr}{Ra}} \frac{1}{Pr_m} \left\langle \frac{\partial b_i}{\partial x_j} \frac{\partial b_i}{\partial x_j} \right\rangle
 \end{aligned} \tag{2.9}$$

Here  $\langle \cdot \rangle$  denote average over the entire volume. The volume-averaged total heat flux and vertical buoyant energy-flux are denoted by  $q$  and  $\langle u_3\theta \rangle$ . Subscript "0" is used to represent the properties without magnetic field (RC cases) in the rest of this paper.

### 3. Result

We begin the analysis by comparing our simulation results for DC and RC in terms of their global heat transfer and turbulence properties. In figure 3, the ratio of the Nusselt number for DC to RC ( $Nu/Nu_0$ ) is plotted with respect to the convective supercriticality ( $\mathcal{R}$ ). The

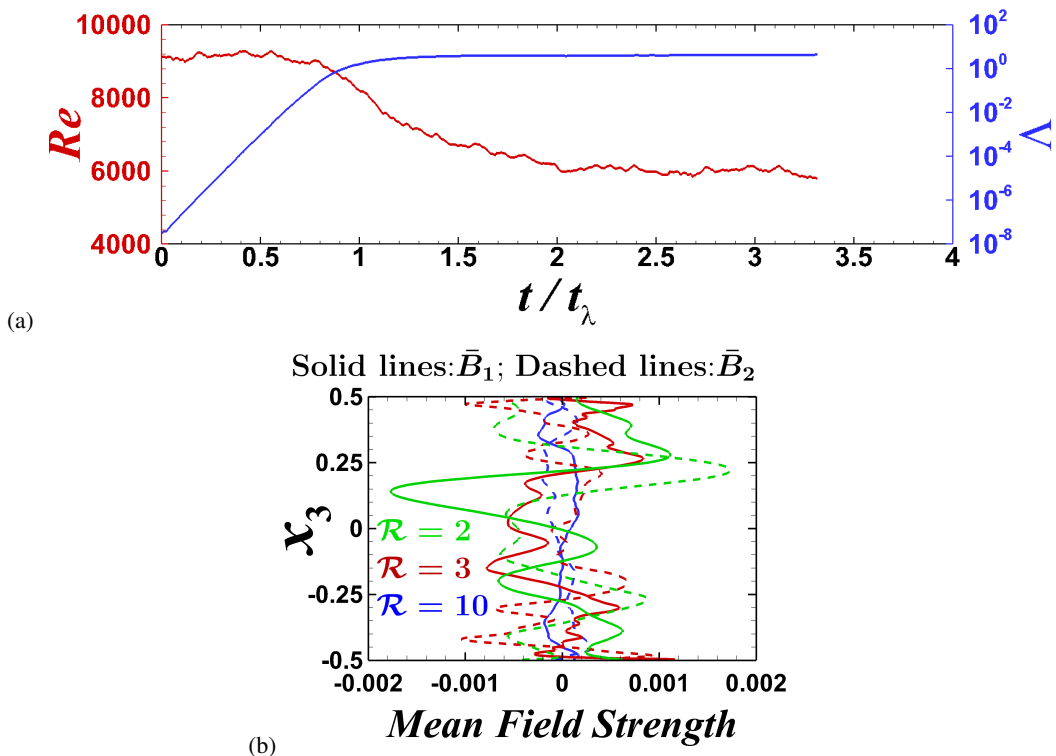


Figure 2: (a) Time evolution of Reynolds Number and Elsasser Number for DC at  $\mathcal{R} = 20$   
 (b) Vertical variation of mean magnetic fields for different  $\mathcal{R}$ .

dynamo action associated with the magnetic field results in increased heat transfer for DC, except at  $\mathcal{R} = 2$ . Maximum enhancement occurs at  $\mathcal{R} = 3$  where the heat transfer of DC is more than 70% as compared to RC. The experiment in a rotating cylinder by King & Aurnou (2015) and the geodynamo simulation in a spherical shell model by Yadav *et al.* (2016) have reported a similar heat transfer enhancement peak. However, this optimum heat transfer enhancement owing to dynamo action is a novel finding for a plane layer dynamo. Interestingly, the peak in heat transfer is found to occur at  $\Lambda \approx 1$  (see table 2), similar to the RMC experiments of King & Aurnou (2015) and the geodynamo simulation of Yadav *et al.* (2016). When the Lorentz force is of similar magnitude with the Coriolis force, the global magnetorelaxation process should enhance heat transport in RMC (King & Aurnou 2015). However, this leading order magnetostrophic balance for  $\Lambda = O(1)$  may not represent the primary balance in DC (Calkins 2018; Soderlund *et al.* 2015; Aurnou & King 2017). The traditional definition of Elsasser number ( $\Lambda = \sigma B_{r.m.s.}^2 / \rho \Omega$ ) gives a correct ratio of the Lorentz and the Coriolis forces only for small  $Re_m \leq O(1)$ , which is not valid for a dynamo (Soderlund *et al.* 2015; Aurnou & King 2017). As the global force balance reported in the simulation (Yadav *et al.* 2016) is geostrophic, not magnetostrophic, a similar magnetorelaxation process as reported in the RMC experiment of (King & Aurnou 2015), may not be the reason for heat transfer enhancement in the DC simulations of (Yadav *et al.* 2016). The present study indicates a local increase in the Lorentz force near the top and bottom plates signifying the importance of the thermal boundary layer dynamics for the heat transfer enhancement in dynamo simulations, instead of any global force balance.

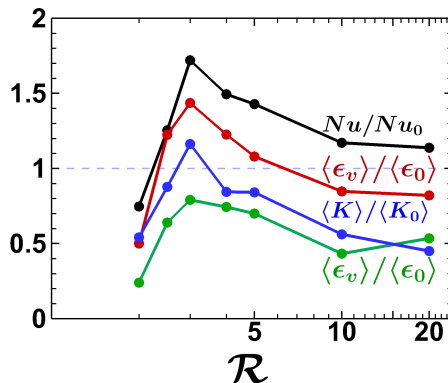


Figure 3: Ratio of Nusselt Number, Turbulent Kinetic Energy, viscous dissipation, and Joule dissipation as a function of convective supercriticality. Subscript “0” is used to represent non-magnetic simulation.

The global statistics of the underlying turbulent motion are shown in figure 3 to understand the heat transfer enhancement phenomenon. We observe that the ratio of the turbulent kinetic energy (*t.k.e.*) of the DC simulations to the RC simulations,  $\langle K \rangle / \langle K_0 \rangle$ , achieves a maximum at  $\mathcal{R} = 3$  indicating higher turbulence intensity in dynamo convection as compared to rotating convection. We further confirm this enhanced turbulence activity by showing the variation of the ratio of viscous dissipation,  $\langle \epsilon_v \rangle / \langle \epsilon_0 \rangle$ , in figure 3. A similar peak in dissipation ratio for  $\mathcal{R} = 3$  is observed. Additionally, the part of kinetic energy converted into magnetic energy dissipates via Joule dissipation. The normalized Joule dissipation of magnetic energy,  $\langle \epsilon_j \rangle / \langle \epsilon_0 \rangle$ , manifests a similar peak. These observations confirm increased turbulence for  $\mathcal{R} = 3$  that promotes mixing and scalar transport, resulting in heat transfer enhancement.

To explore the possible reasons for this increased turbulence and heat transfer enhancement, we can compare the vertical variation of forces in figure 4 for DC and RC with both no-slip and free-slip boundary conditions at  $\mathcal{R} = 3$ . The forces are calculated from the *r.m.s* values of the terms in momentum equation (2.2) by averaging over horizontal planes (Yan *et al.* 2021). The leading order geostrophic balance between pressure and the Coriolis forces are apparent for all cases as shown in figures 4 a, c and e. Geostrophic balance is known to be the characteristic of strongly rotating convection (King *et al.* 2012). Small departures from this balance due to the other forces make quasi-geostrophic convection (even turbulence) possible in such flows, making these other forces important for the dynamics. In the present study, buoyancy, viscous, and inertia constitute the quasi-geostrophic force balance in RC at  $\mathcal{R} = 3$  (see figure 4a). Although the viscous diffusion term is smallest in the bulk, it increases near the Ekman layer at the bottom plate as shown in figure 4b and dominates the quasi-geostrophic balance. For the no-slip boundary condition, the velocities are zero at the wall, which results in an increase in the pressure force at the walls (figure 4b,d). In figure 4c, the Lorentz force, which is at least one order of magnitude lower than Coriolis force in the bulk, decreases from the wall towards the center of the domain, reaching a minimum. Therefore, the global magnetostrophic balance between the Lorentz and the Coriolis forces, as found in the previous RMC experiment (King & Aurnou 2015), may not be the reason for the heat transfer enhancement in the present DC simulations. A closer look near the bottom plate for DC at  $\mathcal{R} = 3$  reveals a different dynamical behavior in figure 4d. Here, the Lorentz

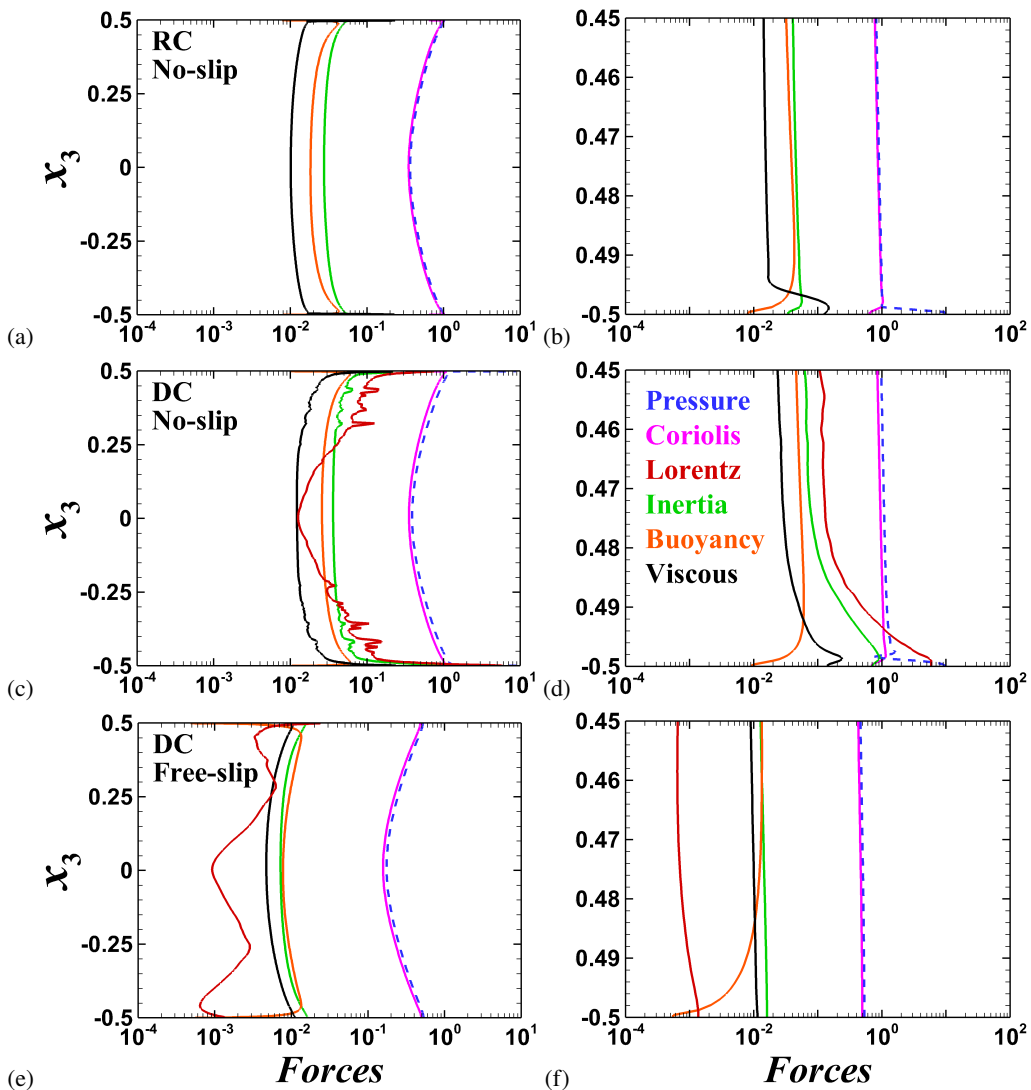


Figure 4: Vertical variation of forces at  $\mathcal{R} = 3$  for (a, b) no-slip RC, (c, d) no-slip DC and (e, f) free-slip DC. The horizontally averaged force distribution is shown in the bulk(left column) and near the bottom plate(right column).

force increases nearly three orders of magnitude from its value at the center of the domain to become the dominant force at the wall. This increase in the Lorentz force near the wall can attenuate the turbulence suppressing effect of the Coriolis force resulting in enhanced turbulence, mixing, and heat transfer. We also observe a similar increase in Lorentz force near the boundary for  $\mathcal{R} = 2.5, 4$  and  $5$  (figures not shown). Apart from a dissimilar vertical variation, the Lorentz force for the free-slip boundary condition case (figure 4e) is one order of magnitude lower compared to the no-slip boundary condition case (figure 4c). Furthermore, no enhancement in the Lorentz force is observed for the free-slip boundary condition case near the wall (see figure 4f).

Further analysis on the boundary layer characteristics can be made to assess the relative

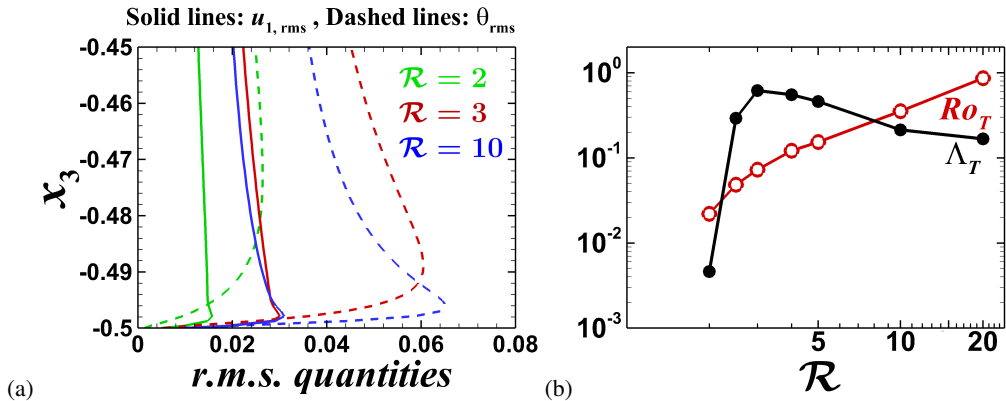


Figure 5: (a) Horizontal *r.m.s* velocity (solid lines) and temperature profiles (dashed lines) near wall for DC cases, (b) variation of local Elsasser and the Rossby number at the thermal boundary layer edge with convective supercriticality.

magnitudes of the Lorentz and the Coriolis forces near the walls. The variation of the *r.m.s.* horizontal velocity ( $u_{1,r.m.s}$ ), and the *r.m.s.* temperature ( $\theta_{r.m.s}$ ) in the vertical direction near the bottom plate is shown in figure 5a for DC cases at  $\mathcal{R} = 2, 3$  and 10. Here, we can define the Ekman boundary layer (EBL) and thermal boundary layer (TBL) as the regions adjacent to the plates where viscous, and thermal diffusion are important. In strongly rotating convection, heat is transported by columnar structures, and plumes that are formed due to the instability of the TBL (King *et al.* 2012). The heat transfer characteristics of such systems depend on the relative thickness of the two layers (King *et al.* 2009, 2012). The distance of the peaks in *r.m.s.* horizontal velocity, and temperature from the bottom boundary can be used to estimate the EBL and TBL thickness ( $\delta_E$  and  $\delta_T$ ) respectively from figure 5a (King *et al.* 2009). If  $\delta_T > \delta_E$ , the strong Coriolis force stabilizes the thermal layer, impeding the formation of plumes and thereby restricting heat transfer (King *et al.* 2012). The thermal boundary layer thickness is higher than the Ekman layer for the DC cases as demonstrated in figure 5a. Similar observations are true for RC cases (figure not shown) indicating a strong stabilizing effect of Coriolis force in all simulations. To determine the effect of the Lorentz force in DC cases, we define a local Elsasser number ( $\Lambda_T$ ) at the edge of TBL that measures the ratio of the Lorentz and the Coriolis forces at this location. We emphasize here that this Elsasser number is computed directly from the *r.m.s.* magnitudes of the forces (see figure 4), not from the traditional definition ( $\Lambda$ ). The variation of  $\Lambda_T$  with  $\mathcal{R}$  at the TBL edge near the bottom boundary is shown in figure 5b. The two forces can be seen to be of the same order of magnitude near the edge of the TBL for  $\mathcal{R} = 2.5, 3, 4$  and 5. The local Elsasser number also achieves a maximum at  $\mathcal{R} = 3$ , similar to the Nusselt number ratio (see figure 3), indicating a correlation between the increase in the Lorentz force and the heat transport behavior. The increase in the Lorentz force at the thermal boundary layer effectively mitigates the stabilizing effect of the Coriolis force and can be seen as a local magnetorelaxation of the Taylor-Proudman constraint, resulting in enhanced turbulence and heat transport. Though the inertia force, represented by the Rossby Number ( $Ro_T$ , the ratio of inertia to Coriolis force) in figure 5b, also increases near the wall, the monotonically increasing trend does not correlate with the heat transfer behavior.

To corroborate the local magnetorelaxation process, and enhancement in turbulence, we show the vertical variation of viscous dissipation ratio ( $\bar{\epsilon}_v/\bar{\epsilon}_0$ ) near the bottom wall in figure 6a. This dissipation ratio is computed after averaging the dissipation for DC, and RC

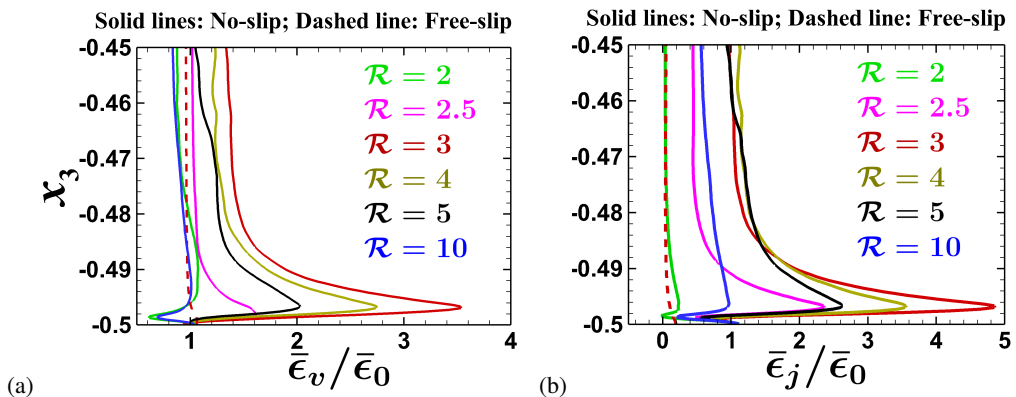


Figure 6: Vertical variation of (a) viscous dissipation ratio, and (b) Joule dissipation ratio near the bottom plate for DC cases with no-slip (solid lines) and free-slip (dashed line) boundary conditions.

simulations over the horizontal directions. We observe an increase in viscous dissipation for  $\mathcal{R} = 2.5, 3, 4$  and  $5$ , near the bottom boundary, suggesting an increase in turbulence near the walls because of the local magnetorelaxation. This enhancement in viscous dissipation is highest for  $\mathcal{R} = 3$  indicating higher turbulence intensity among all the other cases. Similar enhancement in Joule dissipation can also be observed in figure 6b. However, no such enhancement in viscous and Joule dissipation is found at  $\mathcal{R} = 3$  for free-slip boundary condition (dashed lines).

Isosurfaces of temperature perturbation for DC (left column) and RC (right column) are shown in figure 7 to provide visualizations of the thermal structures. The horizontally averaged temperature variation is subtracted from the instantaneous temperature field to compute these temperature perturbations. For RC, the flow morphology changes from columnar cells at  $\mathcal{R} = 2$  (figure 7b) to plumes at  $\mathcal{R} = 3$  (figure 7d) to geostrophic turbulence dominating at larger thermal forcing at  $\mathcal{R} = 10$  (figure 7f). The transition of flow morphology from columnar cells to plumes occur at  $RaE^{4/3} \sim 22$  whereas the transition from plumes to geostrophic turbulence happens at  $RaE^{4/3} \sim 55$  (Julien *et al.* 2012). For the present RC simulations at  $\mathcal{R} = 2, 3$  and  $10$ , the values of  $RaE^{4/3} = 15.2, 22.8$  and  $76$ , agrees well with the predictions of this transition regime. Thick columnar convection cells with larger horizontal scales are observed for DC at  $\mathcal{R} = 2$  in figure 7a, due to higher effective viscosity in the presence of a magnetic field (Chandrasekhar 1961). The temperature perturbation field at  $\mathcal{R} = 3$  constitutes both columnar structures, and plumes as shown in figure 7c and figure 7d. Compared to RC in figure 7d, DC at  $\mathcal{R} = 3$  (figure 7c) is more populated by columnar structures, and plumes. This increased population of columnar structures and plumes is expected due to the local magnetorelaxation phenomenon near the thermal boundary layer as reported in figures 5 and 6. The upwards (downwards) motion of the hot(cold) plumes from the bottom(top) wall towards the bulk transport momentum, and thermal energy to increase turbulence and heat transport, as depicted in figure 3. The horizontal distortion of the thermal structures in figure 7c also indicates the relaxation of the Taylor-Proudman constraint due to the magnetic field. Convection at  $\mathcal{R} = 10$  occurs in the geostrophic turbulence regime, as apparent from figures 7e,f with more turbulence and abundant small scale structures as compared to lower  $\mathcal{R}$  cases.

We now look into the reason for the enhancement of Lorentz force at the thermal boundary

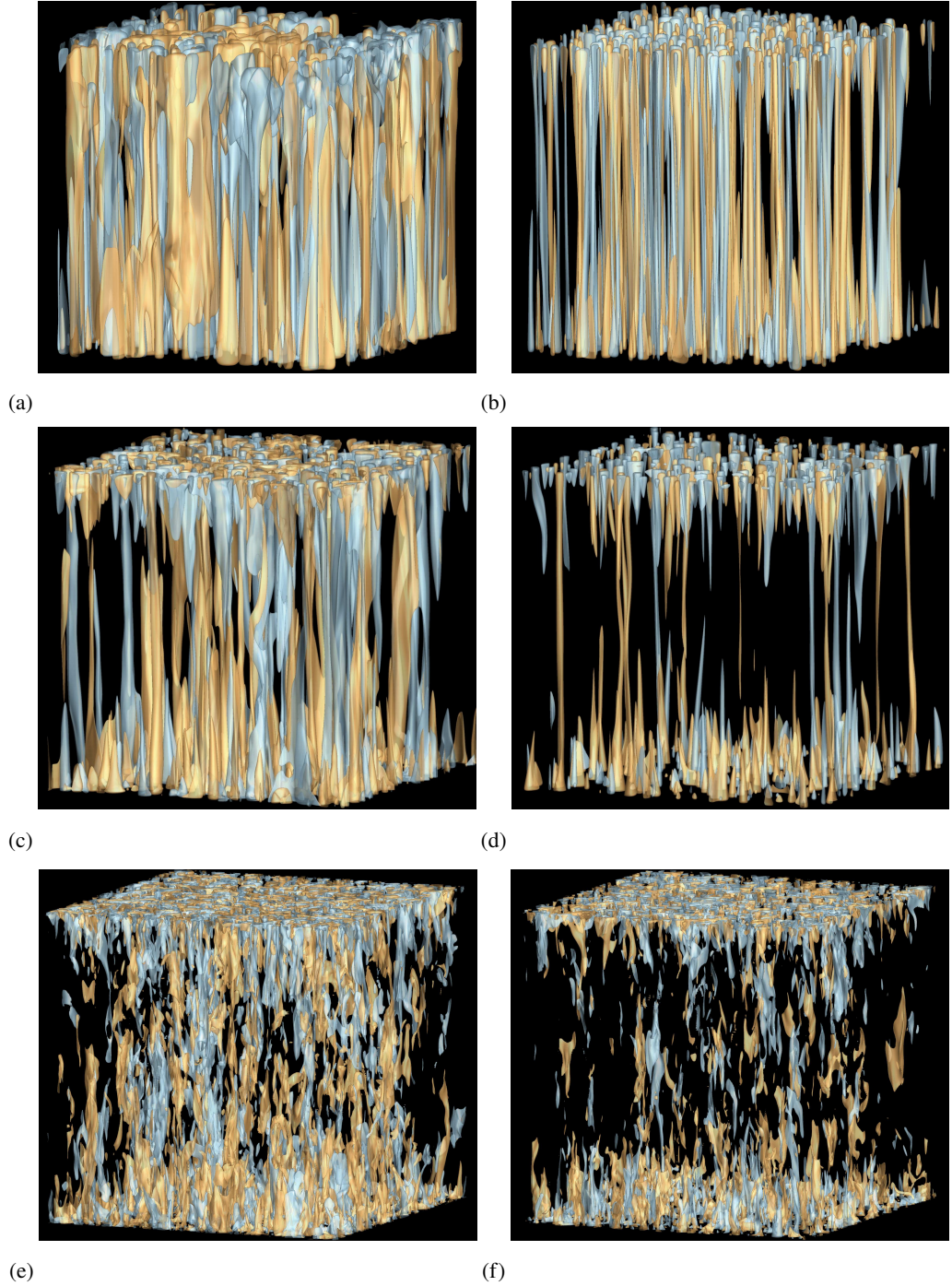


Figure 7: Isosurfaces of temperature perturbation for DC (left column) and RC cases (right column). Hot (orange) and cold (grey) columnar and plume structures are visualized by isosurface values  $\pm 0.03$  for  $\mathcal{R} = 2$  (a,b),  $\pm 0.07$  for  $\mathcal{R} = 3$  (c,d) and  $\pm 0.07$   $\mathcal{R} = 10$  (e,f).

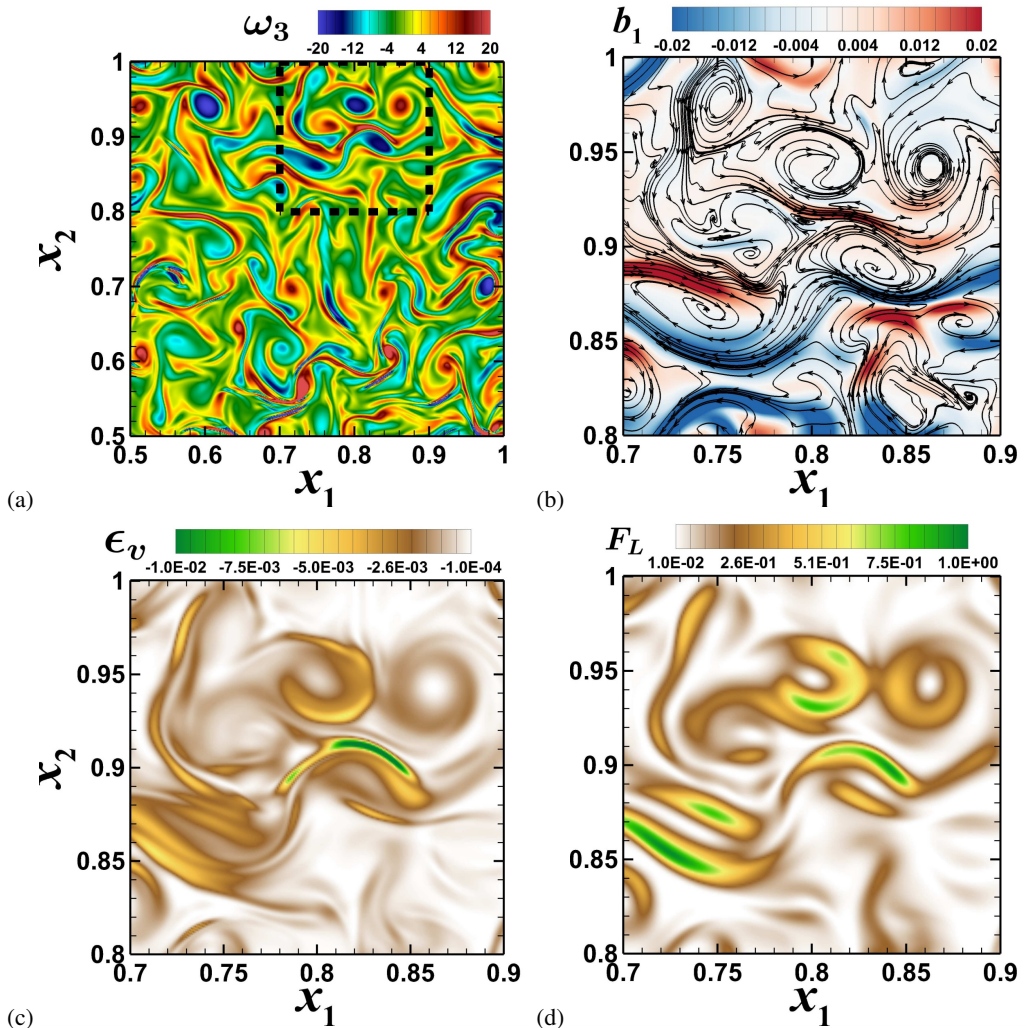


Figure 8: Instantaneous snapshots for horizontal planes of (a) vertical vorticity, (b) magnetic field in  $x_1$ -direction superimposed with magnetic field lines, (c) viscous dissipation, and (d) Lorentz force magnitude. A quarter of the plane is plotted inside the thermal boundary layer ( $x_3 = -0.495$ ) for no-slip DC simulation with  $\mathcal{R} = 3$  in (a). The section marked by the black dashed line in (a) is enhanced in (b), (c) and (d)

layer for DC at  $\mathcal{R} = 3$  with no-slip boundary condition (figure 4d). A quarter of the horizontal plane inside the thermal boundary layer  $x_3 = -0.495$  is plotted in figure 8 to depict the instantaneous vertical vorticity ( $\omega_3$ ). The section surrounded by the black dashed line in the vorticity contour plot (figure 8a) is focused in figures 8b,c and d to show the magnetic field strength in  $x_1$ -direction (i.e.,  $b_1$ , superimposed with magnetic field lines), the viscous dissipation and the Lorentz force magnitude respectively. Comparison of the vorticity and the dissipation contours (figure 8a and c) exhibit the interaction among vortices that leads to shear layers with intense dissipation around the core of the vortices. The magnetic field lines are observed to concentrate around the edges of these vortices (figure 8b). This behavior of the magnetic field can be understood from the flux expulsion mechanism (Weiss 1966; Gilbert *et al.* 2016), where magnetic field lines are advected towards the edges of a vortex.

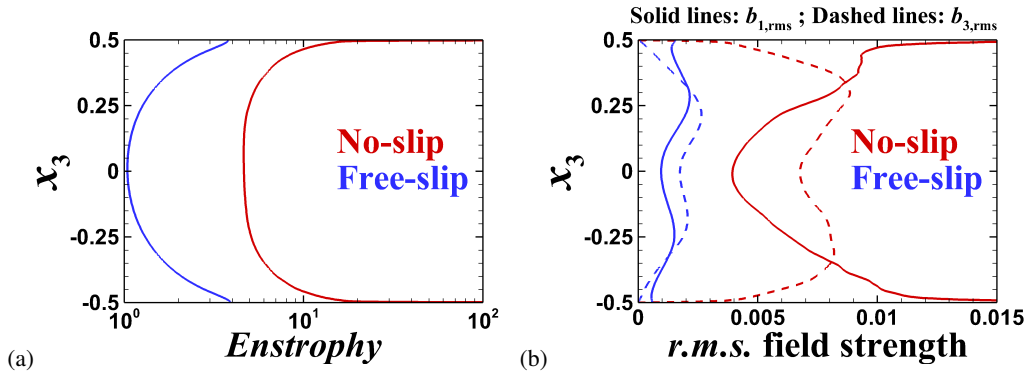


Figure 9: Comparison of results for DC at  $\mathcal{R} = 3$  between no-slip and free-slip conditions: (a) enstrophy and (b) *r.m.s* field strength. Vertical variations are presented after averaging all quantities in the horizontal planes.

These magnetic field lines around the vortices are stretched due to shear leading to the amplification of the magnetic field, hence resulting in a localized increase (figure 8d) in the Lorentz force.

Interestingly, the dynamo behavior for DC at  $\mathcal{R} = 3$  with no-slip and free-slip boundary conditions are found to be very different. In figure 9a strength of the vortices (represented by the horizontally averaged enstrophy,  $1/2 \overline{\omega_i \omega_i}$ ) are an order of magnitude higher near the walls for no-slip boundary condition case as compared to the free-slip boundary condition case. This increase may be attributed to Ekman pumping (Hopfinger & Van Heijst 1993). Apart from higher vertical *r.m.s* magnetic field strength ( $b_{3,rms}$ ), an amplification in horizontal magnetic field strength in  $x_1$  direction ( $b_{1,rms}$ ) is also observed near the wall for the case with no-slip boundary condition in comparison to the case with free-slip boundary condition (see figure 9b). Because of higher enstrophy, the stretching of magnetic field lines by these vortices, and consequently the increase in the Lorentz force near the walls, are higher with no-slip boundary conditions as compared to free-slip boundary conditions (figure 4d,f). This increase in Lorentz force leads to magnetorelaxation in the thermal boundary layer that promotes turbulence and heat transfer enhancement. We do not observe such enhancement in heat transport with free-slip boundary conditions. It should be noted here that for perfectly conducting boundaries, the *r.m.s* magnetic field has to become parallel to the plates with  $b_{3,rms} \rightarrow 0$  near the walls (figure 9b). As the field can not escape the boundaries, a build-up of Lorentz force can be expected (St Pierre 1993). Investigations with insulated wall boundary conditions will be carried out in the future to check whether this mechanism is exclusive to the present combination of boundary conditions.

#### 4. Conclusions

We have performed turbulence resolving simulations of the plane layer dynamo. Our study reveals the presence of an optimum thermal forcing at which heat transfer in DC is most efficient compared to RC. The novelty of this investigation is in reporting a local increase in the Lorentz force at the thermal boundary layer edge (figure 4d) to be the cause of this enhanced heat transport instead of a global balance between the Lorentz, and the Coriolis forces. This local increase in the Lorentz force subsides the turbulence stabilizing effect of

the Coriolis force, and can be viewed as local magnetorelaxation at the thermal boundary layer. This local magnetorelaxation phenomenon results in an increase in the population of plumes, and columnar structures (figure 7c) that increase the intensity of turbulence, and kinetic energy dissipation, especially near the walls (figure 6). We also demonstrate that the stretching of the magnetic field lines around the vortices near the wall is the reason for this enhanced Lorentz force in the thermal boundary layer (figure 8). Therefore, the present simulations reveal that capturing the boundary layer dynamics is imperative for understanding the heat transfer characteristics in dynamo convection, and therefore, further investigation on the near-wall behavior of dynamos is warranted.

It should be reiterated here that the traditional definition of Elsasser Number,  $\Lambda$ , is unsuitable for dynamo simulations (Soderlund *et al.* 2015; Aurnou & King 2017; Calkins 2018). The Elsasser Number in a dynamo simulation is not an input parameter that can be externally controlled, unlike the low  $Re_m$  magnetoconvection experiments. Therefore, in this study, we choose to plot the heat transfer variation against  $\mathcal{R}$ , which is more common for heat transfer studies on scaling laws of convection with or without rotation or magnetic field (Plumley & Julien 2019). The enhancement of heat transfer at lower values of  $\mathcal{R}$  indicates a change of scaling law in strongly rotating convection due to the dynamo action. This parameter choice will help in designing future experiments to facilitate the search for heat transfer scaling laws for dynamo convection.

**Acknowledgements.** The computational support provided by PARAM Sanganak under the National Supercomputing Mission, Government of India at the Indian Institute of Technology, Kanpur is gratefully acknowledged.

**Declaration of interests.** The authors report no conflict of interest.

**Author contributions.** The authors contributed equally to analyzing data and reaching conclusions, and in writing the paper.

## REFERENCES

- AUBERT, J. 2019 Approaching earth’s core conditions in high-resolution geodynamo simulations. *Geophys. J. Int.* **219** (Supplement\_1), S137–S151.
- AURNOU, J.M. & KING, E.M. 2017 The cross-over to magnetostrophic convection in planetary dynamo systems. *Proc. R. Soc. Lond. A Math Phys. Sci.* **473** (2199), 20160731.
- AURNOU, J.M. & OLSON, P.L. 2001 Experiments on Rayleigh–Bénard convection, magnetoconvection and rotating magnetoconvection in liquid gallium. *J. Fluid Mech.* **430**, 283–307.
- BAKHUIS, D., OSTILLA-MÓNICO, R., VAN DER POEL, E.P., ERWIN, P., VERZICCO, R. & LOHSE, D. 2018 Mixed insulating and conducting thermal boundary conditions in Rayleigh–Bénard convection. *J. Fluid Mech.* **835**, 491–511.
- BRACKBILL, J.U. & BARNES, D.C. 1980 The effect of nonzero  $\nabla \cdot \mathbf{B}$  on the numerical solution of the magnetohydrodynamic equations. *J. Comput. Phys.* **35**, 426–430.
- BRUCKER, K.A. & SARKAR, S. 2010 A comparative study of self-propelled and towed wakes in a stratified fluid. *J. Fluid Mech.* **652**, 373–404.
- CALKINS, M.A. 2018 Quasi-geostrophic dynamo theory. *Physics of the Earth and Planetary Interiors* **276**, 182–189.
- CALKINS, M.A., JULIEN, K., TOBIAS, S.M. & AURNOU, J.M. 2015 A multiscale dynamo model driven by quasi-geostrophic convection. *J. Fluid Mech.* **780**, 143–166.
- CATTANEO, F. & HUGHES, D.W. 2006 Dynamo action in a rotating convective layer. *J. Fluid Mech.* **553**, 401–418.
- CHANDRASEKHAR, S. 1961 *Hydrodynamic and hydromagnetic stability*. Courier Corporation.
- CHRISTENSEN, U.R. & WICHT, J. 2015 Numerical dynamo simulations. In *Treatise on Geophysics (Second Edition), Volume 8: Core Dynamics* (ed. Peter Olson), pp. 245–277. Elsevier.

- ELTAYEB, I.A. 1972 Hydromagnetic convection in a rapidly rotating fluid layer. *Proceedings of the Royal Society of London. A. Mathematical and Physical Sciences* **326**, 229–254.
- FAVIER, B. & BUSHBY, P.J. 2013 On the problem of large-scale magnetic field generation in rotating compressible convection. *J. Fluid Mech.* **723**, 529–555.
- GILBERT, A.D., MASON, J. & TOBIAS, S.M. 2016 Flux expulsion with dynamics. *J. Fluid Mech.* **791**, 568–588.
- GLATZMAIERS, G.A. & ROBERTS, P.H. 1995 A three-dimensional self-consistent computer simulation of a geomagnetic field reversal. *Nature* **377** (6546), 203–209.
- GUERVILLY, C., HUGHES, D.W. & JONES, C.A. 2015 Generation of magnetic fields by large-scale vortices in rotating convection. *Phys. Rev. E.* **91** (4), 041001.
- GUERVILLY, C., HUGHES, D.W. & JONES, C.A. 2017 Large-scale-vortex dynamos in planar rotating convection. *J. Fluid Mech.* **815**, 333–360.
- HOPFINGER, E.J. & VAN HEIJST, G.J.F. 1993 Vortices in rotating fluids. *Ann. Rev. Fluid Mech.* **25** (1), 241–289.
- HUGHES, D.W. & CATTANEO, F. 2019 Force balance in convectively driven dynamos with no inertia. *J. Fluid Mech.* **879**, 793–807.
- IYER, K.P., SCHEEL, J.D., SCHUMACHER, J. & SREENIVASAN, K.R. 2020 Classical 1/3 scaling of convection holds up to  $Ra = 10^{15}$ . *Proc. Natl. Acad. Sci. USA* **117** (14), 7594–7598.
- JONES, C.A. & ROBERTS, P.H. 2000 Convection-driven dynamos in a rotating plane layer. *J. Fluid Mech.* **404**, 311–343.
- JULIEN, K., RUBIO, A.M., GROOMS, I. & KNOBLOCH, E. 2012 Statistical and physical balances in low Rossby number Rayleigh–Bénard convection. *Geophysical & Astrophysical Fluid Dynamics* **106** (4-5), 392–428.
- KÄPYLÄ, P.J., KORPI, M.J. & BRANDENBURG, A. 2009 Alpha effect and turbulent diffusion from convection. *Astronomy & Astrophysics* **500** (2), 633–646.
- KING, E.M. & AURNOU, J.M. 2015 Magnetostrophic balance as the optimal state for turbulent magnetoconvection. *Proc. Natl. Acad. Sci. USA* **112** (4), 990–994.
- KING, E.M., STELLMACH, S. & AURNOU, J.M. 2012 Heat transfer by rapidly rotating Rayleigh–Bénard convection. *J. Fluid Mech.* **691**, 568–582.
- KING, E.M., STELLMACH, S., NOIR, J., HANSEN, U. & AURNOU, J.M. 2009 Boundary layer control of rotating convection systems. *Nature* **457** (7227), 301–304.
- MOFFATT, K. & DORMY, E. 2019 *Self-exciting fluid dynamos*. Cambridge University Press.
- MONCHAUX, R., BERHANU, M., BOURGOIN, M., MOULIN, M., ODIER, PH., PINTON, J.-F., VOLK, R., FAUVE, S., MORDANT, N., PÉTRÉLIS, F. & OTHERS 2007 Generation of a magnetic field by dynamo action in a turbulent flow of liquid sodium. *Phys. Rev. Lett.* **98** (4), 044502.
- NAKAGAWA, Y. 1957 Experiments on the instability of a layer of mercury heated from below and subject to the simultaneous action of a magnetic field and rotation. *Proceedings of the Royal Society of London. Series A. Mathematical and Physical Sciences* **242**, 81–88.
- NAKAGAWA, Y. 1959 Experiments on the instability of a layer of mercury heated from below and subject to the simultaneous action of a magnetic field and rotation. ii. *Proceedings of the Royal Society of London. Series A. Mathematical and Physical Sciences* **249**, 138–145.
- NIMMO, F. 2015 Energetics of the Core. In *Treatise on Geophysics (Second Edition), Volume 8: Core Dynamics* (ed. Peter Olson), pp. 27–56. Elsevier.
- PAL, A. & CHALAMALLA, V.K. 2020 Evolution of plumes and turbulent dynamics in deep-ocean convection. *J. Fluid Mech.* **889**, A35.
- PAL, A. & SARKAR, S. 2015 Effect of external turbulence on the evolution of a wake in stratified and unstratified environments. *J. Fluid Mech.* **772**, 361–385.
- PAL, A., DE STADLER M.B. & S., SARKAR 2013 The spatial evolution of fluctuations in a self-propelled wake compared to a patch of turbulence. *Phys. Fluids* **25**, 095106.
- PHAM, H.T., SARKAR, S. & BRUCKER, K.A. 2009 Dynamics of a stratified shear layer above a region of uniform stratification. *J. Fluid Mech.* **630**, 191–223.
- PLUMLEY, M. & JULIEN, K. 2019 Scaling laws in Rayleigh-Benard convection. *Earth and Space Science* **6** (9), 1580–1592.
- ROBERTS, P.H. & KING, E.M. 2013 On the genesis of the earth’s magnetism. *Reports on Progress in Physics* **76** (9), 096801.
- ROTVIG, J. & JONES, C.A. 2002 Rotating convection-driven dynamos at low Ekman number. *Phys. Rev. E.* **66** (5), 056308.

- SCHMITZ, S. & TILGNER, A. 2009 Heat transport in rotating convection without Ekman layers. *Phys. Rev. E* **80** (1), 015305.
- SCHWAIGER, T., GASTINE, T. & AUBERT, J. 2019 Force balance in numerical geodynamo simulations: a systematic study. *Geophysical Journal International* **219** (Supplement\_1), S101–S114.
- SODERLUND, K.M., SHEYKO, A., KING, E.M. & AURNOU, J.M. 2015 The competition between Lorentz and Coriolis forces in planetary dynamos. *Progress in Earth and Planetary Science* **2** (1), 1–10.
- ST PIERRE, M.G. 1993 The strong field branch of the Childress-Soward dynamo. In *Solar and Planetary Dynamos* (ed. M.R.E. Proctor & A.D. Gilbert), pp. 245–277. Cambridge University Press.
- STELLMACH, S. & HANSEN, U. 2004 Cartesian convection driven dynamos at low Ekman number. *Phys. Rev. E* **70** (5), 056312.
- STELLMACH, S., LISCHPER, M., JULIEN, K., VASIL, G., CHENG, J.S., RIBEIRO, A., KING, E.M. & AURNOU, J.M. 2014 Approaching the asymptotic regime of rapidly rotating convection: boundary layers versus interior dynamics. *Phys. Rev. Lett.* **113** (25), 254501.
- STEVENSON, D.J. 1979 Turbulent thermal convection in the presence of rotation and a magnetic field: a heuristic theory. *Geophysical & Astrophysical Fluid Dynamics* **12** (1), 139–169.
- TILGNER, A. 2012 Transitions in rapidly rotating convection driven dynamos. *Phys. Rev. Lett.* **109** (24), 248501.
- TILGNER, A. 2014 Magnetic energy dissipation and mean magnetic field generation in planar convection-driven dynamos. *Phys. Rev. E* **90** (1), 013004.
- WEISS, N.O. 1966 The expulsion of magnetic flux by eddies. *Proc. R. Soc. Lond. A Math Phys. Sci.* **293** (1434), 310–328.
- YADAV, R.K., GASTINE, T., CHRISTENSEN, U.R., WOLK, S.J. & POPPENHAEGER, K. 2016 Approaching a realistic force balance in geodynamo simulations. *Proc. Natl. Acad. Sci. USA* **113** (43), 12065–12070.
- YAN, M., CALKINS, M. A., MAFFEI, S., JULIEN, K., TOBIAS, S.M. & MARTI, P. 2019 Heat transfer and flow regimes in quasi-static magnetoconvection with a vertical magnetic field. *J. Fluid Mech.* **877**, 1186–1206.
- YAN, M., TOBIAS, S.M. & CALKINS, M.A. 2021 Scaling behaviour of small-scale dynamos driven by Rayleigh–Bénard convection. *J. Fluid Mech.* **915**.